Volume 21
Number 34
14 September 2025
Pages 6651–6824

Soft Matter

rsc.li/soft-matter-journal

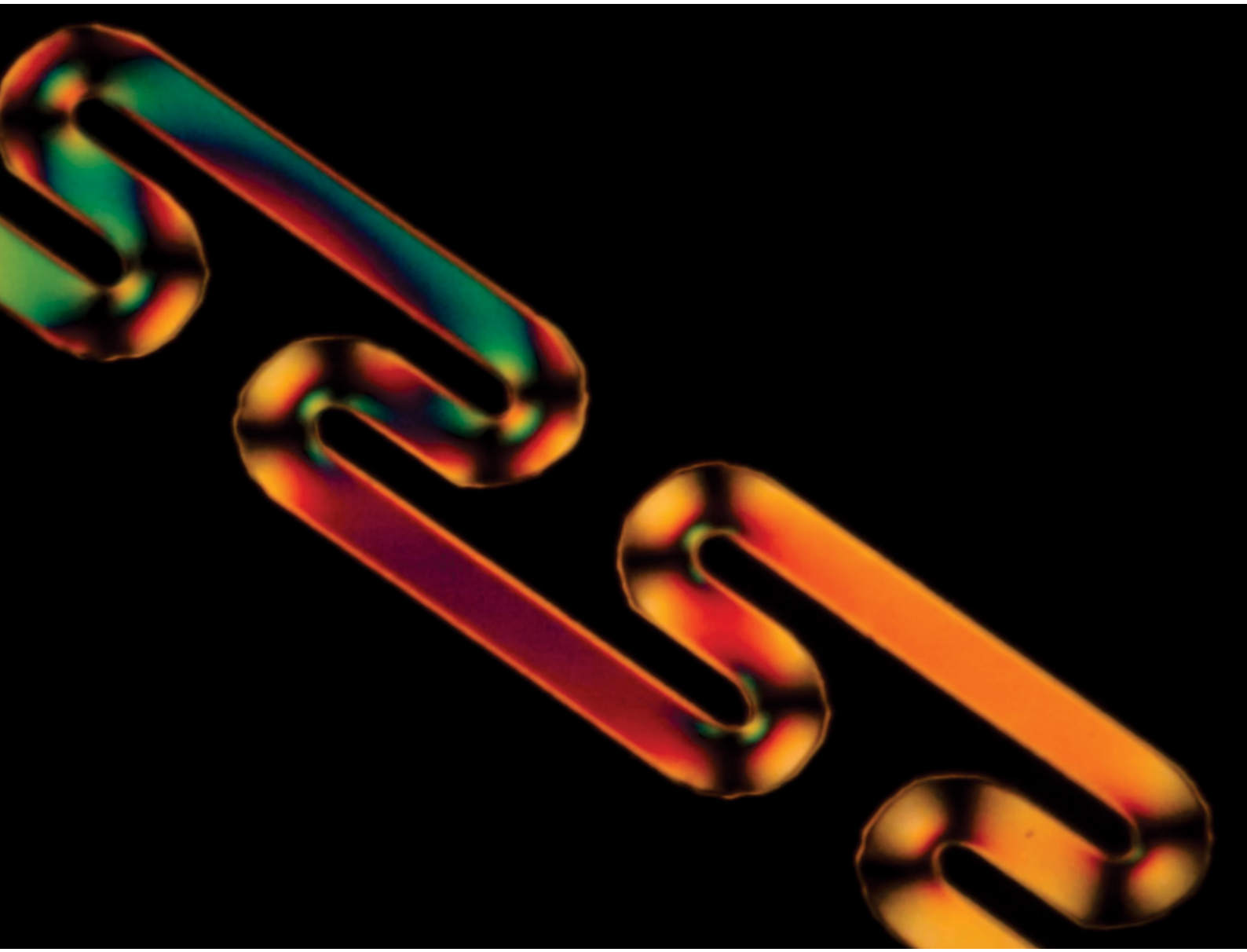

ISSN 1744-6848

ROYAL SOCIETY OF CHEMISTRY

PAPER
Uroš Tkalec *et al.*
Microchannel geometry effects on nematic dowser domain dynamics

20 YEARS ANNIVERSARY

Soft Matter

PAPER

View Article Online
View Journal | View Issue

Cite this: *Soft Matter*, 2025, **21**, 6679

Microchannel geometry effects on nematic dowser domain dynamics†

Tadej Emeršič, [ai] Rui Zhang, [b] Simon Čopar, [c] Juan J. de Pablo [ade] and Uroš Tkalec *[fgh]

Received 30th May 2025,
Accepted 16th July 2025

DOI: 10.1039/d5sm00562k

rsc.li/soft-matter-journal

Understanding the dynamics of topological defects in liquid crystals is essential for optimizing their performance in adaptive optics, responsive surfaces, and advanced display technologies. Here, we investigate the dynamics of disclination loops enclosing an escaped structure in a nematic liquid crystal, known as dowser domains, within microfluidic channels of various geometries. Through a combination of experiments and numerical simulations, we demonstrate that fluid flow, dictated by the channel geometry alone, governs the dynamics, shape, and size of these domains. We find that channel constrictions extend the lifetime of dowser domains by accelerating their growth, while channel expansions slow down their dynamics and shorten their lifetime. In addition, manipulating the flow paths of dowser domains through serpentine microchannels can further influence their shape and lifespan. We also demonstrate domain splitting in a T-junction microchannel. These findings pave the way for the design of hierarchical networks that can manipulate dowser domains in high-throughput parallel channel systems. Taken together, the results presented here improve our understanding of defect loop dynamics in soft materials and advance the development of flow-based liquid crystal devices and applications.

1. Introduction

Controlling fluid flow at the micron scale provides a highly versatile approach for manipulating the structures and dynamics of complex fluids and soft materials.[1–5] The resulting shear forces allow precise control over arrangement, orientation, and morphology, potentially driving phase transitions and structural transformations in polymers,[6] colloidal particles,[7] and liquid crystals (LCs).[8–11] In emulsions and foams, where distinct phases of one fluid are dispersed within another, fluid flow and shear forces play a crucial role in determining droplet size, shape, and distribution.[12,13] Similarly, in gels[14] and soft solids,[15] which exhibit solid-like behavior at low stresses but flow at higher stresses, fluid flow influences the formation of network structures and the material's mechanical properties. Fluid dynamics on the micron scale is also of fundamental importance for the design of advanced microfluidic devices and for the enhancement of applications in biomedical research and material science.[16,17]

Nematic LCs (NLCs) are ideal candidates for studying and harnessing the effects of fluid flow at the microscale due to their unique combination of fluidity and crystalline properties.[10,18–20] The long-range orientational order of LC molecules results in optical and elastic anisotropy,[21,22] making NLCs highly responsive to external stimuli such as shear forces and electric fields. Under non-equilibrium conditions, these stimuli can induce the formation of metastable structures[23,24] that often contain topological defects – regions where the molecular orientation is undefined. These defects, which can appear as points, lines, or closed loops,[25] play a crucial role in the structural and dynamical properties of the material.[26,27] Beyond their fundamental importance, topological defects have been harnessed as templates for molecular self-assembly[28] and material transport.[29] The ability to create and manipulate such

[a] *Pritzker School of Molecular Engineering, University of Chicago, Chicago, IL 60637, USA*
[b] *Department of Physics, Hong Kong University of Science and Technology, Clear Water Bay, Kowloon, Hong Kong SAR*
[c] *Faculty of Mathematics and Physics, University of Ljubljana, 1000 Ljubljana, Slovenia*
[d] *Materials Science Division, Argonne National Laboratory, Lemont, IL 60439, USA*
[e] *Department of Chemical and Biological Engineering, Computer Science, and Physics, Tandon School of Engineering and Courant Institute of Mathematical Sciences, New York University, New York, NY 10012, USA*
[f] *Institute of Biophysics, Faculty of Medicine, University of Ljubljana, 1000 Ljubljana, Slovenia. E-mail: uros.tkalec@mf.uni-lj.si*
[g] *Faculty of Natural Sciences and Mathematics, University of Maribor, 2000 Maribor, Slovenia*
[h] *Department of Condensed Matter Physics, Jožef Stefan Institute, 1000 Ljubljana, Slovenia*
[i] *Department of Physics and Materials Science, University of Luxembourg, 162a avenue de la Faiencerie, L-1511 Luxembourg*

† Electronic supplementary information (ESI) available. See DOI: https://doi.org/10.1039/d5sm00562k

metastable structures and defects with precision can be further enhanced by microfluidics, which provides a controlled environment to explore the dynamics of defects and material behavior.[18,30–33]

The fluid dynamics of NLCs has been studied for several decades.[30,34–36] The flow of LCs is coupled with their nematic orientational order, resulting in significant local reorientations of the director and the formation of topological defects. Flow-induced reorientation of LC molecules influences the optical and mechanical properties of LCs confined in microfluidic environments, impacting the dynamic behavior and transport properties of nematic colloidal suspensions,[37] the rheological response of nematic fluids,[38] and the dynamics of topological defects.[39] Research has focused mainly on modulation of LC flows by surface anchoring and hydrodynamic forces in linear microchannels. More recently, studies have expanded to explore LC flow dynamics in complex microfluidic geometries, such as rectangular channels with obstacles,[40] topological flow junctions,[31] and curvilinear microchannels.[41] Despite these advances, our recent work[18] has demonstrated that linear microchannels remain effective for manipulating defect structures. We have shown that a combination of controlled fluid flow in a linear microchannel and localized laser pulses can generate and stabilize defect loops, known as reconfigurable domains with polar order, or ''dowser domains''.[18] Although considerable progress has been made in the study of dowser domains in simple linear geometries, there is still a gap in our understanding of their dynamics and behavior in more complex microchannels.

In this work, we build on previous work[18] and examine the behavior of nematic dowser domains in microchannels of various geometries. Through a combination of experiments and numerical simulations, we show how controlled fluid flow—dictated solely by channel geometry, such as constriction, expansion, and bend, allows precise manipulation of the dynamics, shape, and size of dowser domains. Our findings reveal that constrictions extend the lifetime of dowser domains by accelerating their growth, whereas expansions decelerate the domains and reduce their lifetime. Altered flow paths within serpentine microchannels can further extend the shape and lifespan of domains. We also observe domain splitting and merging at T-junction microchannels. These findings contribute to the development of hierarchical microfluidic networks capable of guiding and transforming dowser domains with high precision, opening up new opportunities for autonomous soft matter systems and adaptive materials.

2. Methods and materials

2.1. Materials and experimental procedures

The thermotropic LC 5CB (4-cyano-4′-pentylbiphenyl, Synthon Chemicals), which has a nematic phase between 18 and 35 °C, is used for the experiments. 5CB is subject to Poiseuille flow in all microfluidic channel geometries, such as linear, constriction, expansion, serpentine, and T-junction configurations. All channels have a rectangular cross-section with a fixed height of 12 μm and widths from 40 to 200 μm. The microchannels are made of polydimethylsiloxane (PDMS, Sylgard 184, Dow Corning) and bonded to a glass substrate coated with indium tin oxide (ITO) (Xinyan Technology) after both surfaces have been exposed to an oxygen plasma. The ITO coating serves as an absorber for the infrared (IR) laser light and enables precise localized heating of the 5CB. Teflon tubes are inserted at both ends of the microfluidic channels to serve as connectors for the inflow and outflow of the LC. The channel walls are chemically treated with 0.2 wt% aqueous solution of silane dimethyl-octadecyl-3-aminopropyl-trimethoxysilyl chloride (DMOAP, ABCR GmbH) to induce strong homeotropic surface anchoring for 5CB molecules. The microfluidic channels are filled with 5CB in the isotropic phase and then cooled slowly to the nematic phase at room temperature before flow experiments. All experiments are performed at room temperature.

2.2. Polarized optical imaging, pressure-driven flow, and dowser domain nucleation

The experiments are performed under an inverted polarized optical microscope (Nikon, Eclipse Ti-U, CFI Plan 2× and 10× objectives) in transmission mode. We use a laser tweezers setup with an IR laser light of 1064 nm (Aresis, Tweez 200si) integrated into the microscope to precisely heat the NLC locally and to nucleate dowser domains. Nucleation is achieved by locally heating the NLC into the isotropic phase with the laser and then switching it off, allowing the NLC to quench back to the nematic phase. When the NLC is quenched, the initial defect tangle relaxes into a flow-aligned state bounded by a disclination loop, forming the dowser domain, which then evolves with the flow. The flow in the microchannels is precisely controlled by a pressure controller (OB1 MK3, Elveflow). All dowser domains studied in this work are nucleated in a linear 100 μm wide channel at three different flow velocities: 35 μm s^{-1}, 42 μm s^{-1}, and 50 μm s^{-1}, corresponding to the domains stability under the subcritical, critical, and supercritical velocity, respectively. For each velocity, we study the domains formed with sizes corresponding to their critical radii. This is achieved by tuning the laser power (20 to 200 mW) and optimizing the position of the laser beam – neither too far nor too close to the geometrical channel entrance – to ensure that the domains approach the subsequent geometrical channels with their critical radii. After successful formation, the domains enter microchannels with constriction, expansion, serpentine, or T-junction geometries. All experiments are recorded in full HD videos at 30 frames per second using a digital camera (Canon, EOS 750D). The surface area of the domains is analyzed with the EZC1 software (Nikon).

2.3. Numerical simulations

We use a hybrid lattice Boltzmann method (LBM) to simulate the flowing nematic material. The microstructure and the hydrodynamic flow of the nematic are described by a tensorial order parameter $\mathbf{Q}$ and a velocity vector $\mathbf{u}$, respectively. For a uniaxial NLC, $\mathbf{Q} = S(\mathbf{nn} - \mathbf{I}/3)$, where the unit vector $\mathbf{n}$

represents the nematic director field, S is the scalar order parameter of the nematic, and $\mathbf{I}$ is the identity tensor. By introducing the strain-rate tensor $\mathbf{D} = (\nabla\mathbf{u} + (\nabla\mathbf{u})^{\mathrm{T}})/2$ and vorticity tensor $\mathbf{\Omega} = (\nabla\mathbf{u} - (\nabla\mathbf{u})^{\mathrm{T}})/2$, we define an advection term

$$\mathbf{S} = (\xi\mathbf{D} + \mathbf{\Omega}) \cdot \left(\mathbf{Q} + \frac{\mathbf{I}}{3}\right) + \left(\mathbf{Q} + \frac{\mathbf{I}}{3}\right) \cdot (\xi\mathbf{D} - \mathbf{\Omega}) - 2\xi\left(\mathbf{Q} + \frac{\mathbf{I}}{3}\right)(\mathbf{Q}{:}\nabla\mathbf{u}),$$

where ξ is related to the material's aspect ratio. As 5CB is a flow-aligning LC, we set $\xi = 0.8$.

The evolution of the **Q**-tensor is governed by the Beris–Edwards equation:[42]

$$\frac{\partial\mathbf{Q}}{\partial t} + \mathbf{u}\cdot\nabla\mathbf{Q} - \mathbf{S} = \Gamma\mathbf{H}, \tag{1}$$

where Γ is related to the rotational viscosity of the nematic *via* $\gamma_1 = 2S_0{}^2/\Gamma$ with S_0 the equilibrium scalar order parameter,[43] and $\mathbf{H}$ is the molecular field defined as $\mathbf{H} = -\left(\frac{\delta F}{\delta\mathbf{Q}} - \frac{\mathbf{I}}{3}\mathrm{tr}\left(\frac{\delta F}{\delta\mathbf{Q}}\right)\right)$ that drives the system towards thermodynamic equilibrium with a free energy functional $F = \int_{\mathrm{bulk}}(f_{\mathrm{LdG}} + f_{\mathrm{elastic}})\mathrm{d}V + \int_{\mathrm{surf}} f_{\mathrm{surf}}\mathrm{d}S$. The first term is the short-range Landau–de Gennes free energy density, which reads:[21]

$$f_{\mathrm{LdG}} = \frac{A_0}{2}\left(1 - \frac{U}{3}\right)\mathrm{Tr}(\mathbf{Q}^2) - \frac{A_0 U}{3}\mathrm{Tr}(\mathbf{Q}^3) + \frac{A_0 U}{4}(\mathrm{Tr}(\mathbf{Q}^2))^2,$$

where A_0 and U are material constants. The second term is the long-range elastic energy density written as:[44]

$$f_{\mathrm{elastic}} = \frac{1}{2}LQ_{ij,k}Q_{ij,k} + 2q_0L\varepsilon_{ikl}Q_{ij}Q_{lj,k}, \tag{2}$$

where $Q_{ij,k}$ denotes $\partial_k Q_{ij}$, ϵ_{ikl} is the Levi-Civita tensor. Einstein summation convention is assumed in the above expressions. The nematic coherence length is given by $\xi_{\mathrm{N}} = \sqrt{L/A_0}$, which determines the defect core size and serves as the fundamental length scale for our description of the nematic. The uniform surface anchoring is typically modeled by using a Rapini–Papoular-like surface free energy density functional:[44]

$$f_{\mathrm{surf}} = \frac{1}{2}W\sum_{i,j}\left(Q_{ij} - Q_{ij}^0\right)^2,$$

where Q_{ij}^0 is the preferred anchoring alignment. The evolution of the surface **Q**-field is governed by $\frac{\partial\mathbf{Q}}{\partial t} = -\Gamma_{\mathrm{s}}(-L\nu\cdot\nabla\mathbf{Q} - \left(\frac{\delta f_{\mathrm{surf}}}{\delta\mathbf{Q}} - \frac{\mathbf{I}}{3}\mathrm{Tr}\left(\frac{\delta f_{\mathrm{surf}}}{\delta\mathbf{Q}}\right)\right)$,[45] where $\Gamma_{\mathrm{s}} = \Gamma/\xi_N$. The above equation is equivalent to the mixed boundary condition for steady flow given in.[46]

Using the Einstein summation rule, the Navier–Stokes equation for the NLC can be written as:

$$\rho(\partial_t + u_\beta\partial_\beta)u_\alpha = \partial_\beta\Pi_{\alpha\beta} + \eta\partial_\beta\left[\partial_\alpha u_\beta + \partial_\beta u_\alpha + (1 - 3\partial_\rho P_0)\partial_\gamma u_\gamma\delta_{\alpha\beta}\right]. \tag{3}$$

The stress $\mathbf{\Pi}$ is defined as:

$$\begin{aligned}\mathbf{\Pi}_{\alpha\beta} = &-P_0\delta_{\alpha\beta} - \xi H_{\alpha\gamma}\left(Q_{\gamma\beta} + \frac{1}{3}\delta_{\gamma\beta}\right) \\ &- \xi\left(Q_{\alpha\gamma} + \frac{1}{3}\delta_{\gamma\beta}\right)H_{\gamma\beta} + 2\xi\left(Q_{\alpha\beta} + \frac{1}{3}\delta_{\alpha\beta}\right)Q_{\gamma\varepsilon}H_{\gamma\varepsilon} \\ &- \partial_\beta Q_{\gamma\varepsilon}\frac{\delta F}{\delta\partial_\alpha Q_{\gamma\varepsilon}} + Q_{\alpha\gamma}H_{\gamma\beta} - H_{\alpha\gamma}Q_{\gamma\beta},\end{aligned} \tag{4}$$

where η is the isotropic viscosity, and the hydrostatic pressure P_0 is given by[47] $P_0 = \rho T - f_{\mathrm{bulk}}$. The temperature T is related to the speed of sound c_{s} by $T = c_{\mathrm{s}}{}^2$. We solve the evolution equations using the finite difference method. The Navier–Stokes eqn (3) is solved using a lattice Boltzmann method over a D3Q15 grid[48] with a no-slip boundary condition. Our model and implementation have been validated by comparing our simulation results[45,49] in both passive and active nematic systems with predictions using Ericksen–Leslie–Parodi (ELP) theory.[50–53] The material constants for the simulation are the same as in Emeršič *et al.*[18] We used mesh resolution of 10 nm, simulatin a cell of 500 nm thickness, a smaller size than in experiment to make the computation feasible, but with Ericksen numbers matching the experimental range.

3. Results and discussion

3.1. Generation and stability of dowser domains in linear microchannel

All experiments are performed with NLC 5CB flowing through homeotropic microchannels (Fig. 1a). The channels, made of PDMS and bonded to ITO-coated glass substrates, have a rectangular cross-section with a depth of 12 μm and widths ranging from 40 to 200 μm. The ITO coating serves as an absorber of IR laser light and enables precise control of the local heating of 5CB. By inducing a local temperature quench from the isotropic to the nematic phase in the flowing 5CB, a metastable defect loop with a trapped flow-aligned state forms (Fig. 1b). This oriented polar-phase domain, known as the ''dowser state'' due to its Y-shaped director field resembling a wooden dowser's tool, exhibits a director field in the midplane of the channel aligned horizontally with the flow. The director undergoes a half-turn transition from the bottom to the top of the channel (Fig. 1c), with the disclination loop's cross section shifting from −1/2 to +1/2 profile.

In our previous study,[18] we have demonstrated that the formation, growth rate, and shape of dowser domains in a microfluidic channel can be precisely controlled by confinement, flow, and laser pulses. The dynamics of such a disclination loop with radius r can be described by the phenomenological model:[18]

$$\gamma_r\dot{r} = 2(\gamma_1 - \gamma_2)(v\cos\phi - v_{\mathrm{c}}) - \frac{2\pi T}{r} \tag{5}$$

where ϕ is the in-plane angle of the director field, T is the disclination loop tension, γ_r represents the viscosity parameter associated with the drag force on the moving defect line, γ_1 and γ_2 are viscosity parameters, and v is the flow velocity (Fig. 1d and e).

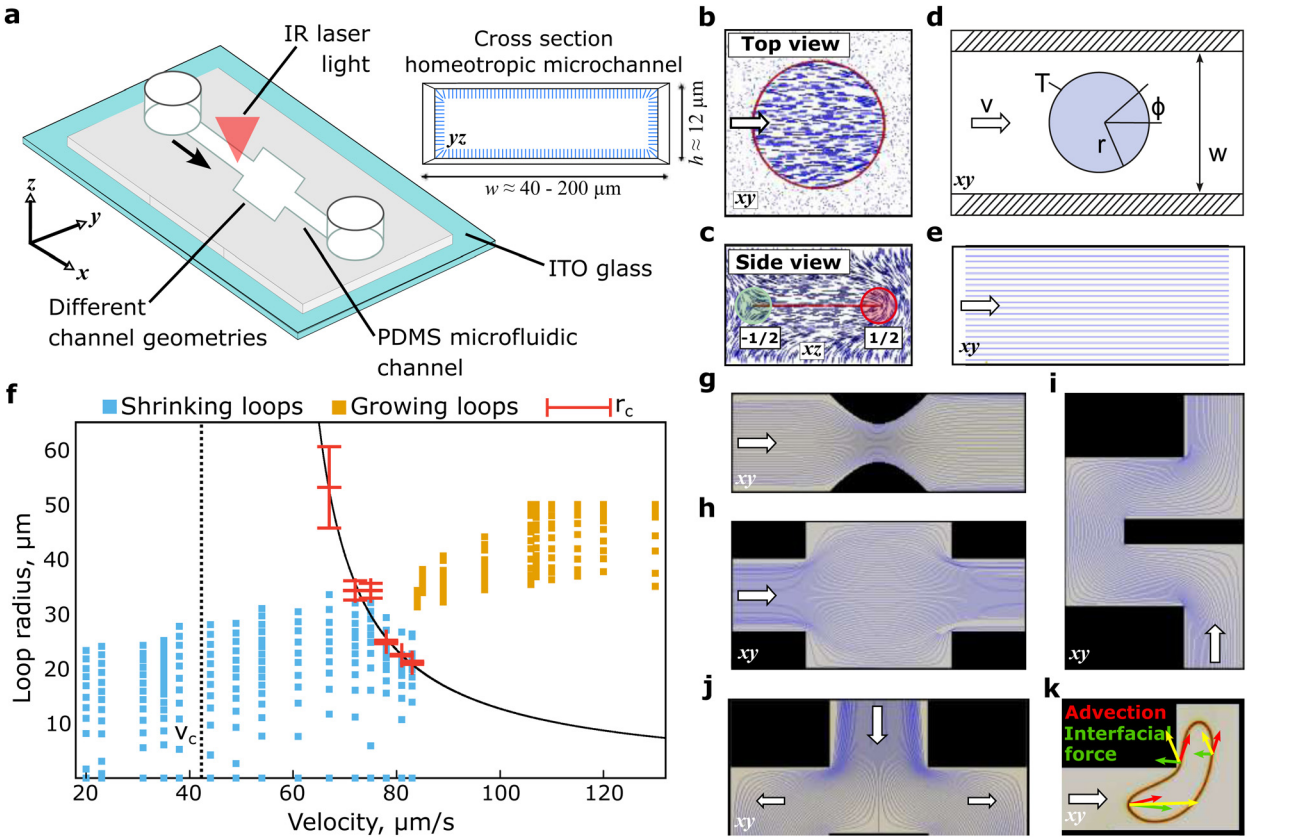

Fig. 1 Dowser domains in microchannels. (a) Schematic representation of a PDMS microfluidic device integrating various channel geometries and a linear microchannel with a rectangular cross-section. Dowser domains are nucleated with an IR laser just before entering the complex geometries. (b) Numerical simulations of a dowser domain stabilized by a half-integer disclination loop, where the entrapped director field aligns with the flow in the midplane. (c) The director field undergoes a half-turn transition from the bottom to the top of the channel. (d) Schematic representation of the dowser domain as described with the 2D quantitative phenomenological model (see eqn (5)). (e) Flow velocity streamlines in a linear microchannel. (f) Phase diagram showing shrinking (blue) and growing (orange) dowser domains, separated by the critical radius curve r_c, in a linear microchannel with a depth of 12 μm and width of 100 μm. (g)–(j) Simulated flow velocity streamlines for different microchannel geometries: (g) constriction, (h) expansion, (i) serpentine, and (j) T-junction. (k) Schematic illustration of the forces acting on a dowser domain, where the advection and interfacial forces from eqn (5) drive the domain propagation.

In a linear microchannel, the dowser domains achieve stability in strong flows but become unstable in weak flows. As the phase diagram in Fig. 1f shows, there is a critical velocity, $v_c = \frac{\pi^3 K}{2h(\gamma_1 - \gamma_2)}$, below which all the dowser domains shrink and eventually annihilate (h is the channel thickness and K is the single elastic constant). Above v_c, the behavior of a dowser domain depends on its initial size. If its radius is smaller than the critical radius, $r_c = \frac{\pi T}{\gamma_1 - \gamma_2}(v - v_c)^{-1}$, disclination tension dominates so that the domain shrinks and disappears. If, on the other hand, $r > r_c$, the domain grows and expands to fill the available space in the channel. For a linear microchannel with a rectangular cross-section, a depth of 12 μm, and a width of 100 μm, the critical velocity v_c, based on the viscoelastic properties of 5CB, is approximately 42 μm s^{-1}.[18]

The behavior of dowser domains in microchannels with complex geometries is still unexplored. The flow profiles in these microchannels can significantly influence the domain dynamics. Here, we investigate constrictions, expansions, serpentines, and T-junction microchannels. In constrictions, the velocity streamlines converge, indicating an increase in fluid velocity due to volume conservation (Fig. 1g). In the case of expansions, on the other hand, the streamlines spread out, which indicates a reduced flow velocity (Fig. 1h). In serpentine bends (Fig. 1i), the separation of streamlines alone is insufficient to determine the flow velocity; instead, a general solution is required that reveals an asymmetric velocity profile with higher speeds near the inner bend wall.[41,54] In a T-junction bifurcated channel, a single velocity streamline splits into two separate channels (Fig. 1j). All dowser domains studied in these complex geometries are first nucleated by a laser beam in a linear microchannel with a rectangular cross-section, a depth of 12 μm, and a width of 100 μm, at three different pressure-driven flow velocities: ≈ 42 μm s^{-1} (critical velocity), ≈ 35 μm s^{-1} (below the critical velocity), and ≈ 50 μm s^{-1} (above the critical velocity). At the time of complete formation, all dowser domains have a size that corresponds to the critical radii (see Methods and materials). After formation, the domains transit from the 100 μm wide linear channel to one of the microchannels with a complex geometry.

All these cases share the inhomogeneous velocity profile. Consequently, we expect disclination loops to be subject to two additional effects (Fig. 1k) that are not accounted for in the simple analysis of a circular domain. First, the advection along the velocity field now reshapes the domains, even without considering forces due to the disclination line tension and free energy differences. Secondly, eqn (5) now acts locally, where r is the local radius of curvature, and $\dot{r}$ is the induced disclination propagation velocity that adds to the advection velocity.

As such, we now expect a generalized propagation in which some parts of the domains can simultaneously grow while others shrink. Fluid flowing around the inner corners of the channels forces the disclination into a concave shape in which the negative radius of curvature causes domain growth even below the critical velocity v_c. This consideration explains all the observations shown in the following sections.

3.2. Dowser domains in constrictions

We design a channel with a constriction in which the linear 100 μm wide channel narrows to about half of its width, which is between 40 and 50 μm (Fig. 2). The length of the constriction region is about 150 μm. As shown both in the numerical simulations and in the experiments (Fig. 2a with Video S1 and Fig. 2b with Video S2, respectively, ESI†), the domain undergoes considerable compression as it passes through the constriction. As the domain approaches the constriction, its front side gradually stretches along the flow direction, while the back side maintains a circular shape. At the narrowest point, the domain reaches its maximum elongation. As it emerges from the constriction, it becomes an ellipse that is significantly larger than its initial size. As the radius of the domain now exceeds the critical threshold, it continues to expand along the channel.

In experiments, variations in flow velocity within the microchannel are observed through changes in the birefringent colors of the NLC.[55] When the domain passes through the constriction, its color changes from green to light red. Simulations show that the director field inside the domain remains predominantly aligned with the flow, suggesting that the color changes are primarily due to variations in domain velocity. Experiments show that a domain nucleated in the linear part of the microchannel at the critical velocity ($\approx$42 μm s^{-1}) passes through the constriction in about 1.1 s (Fig. 2b). This time increases to about 1.4 s for domains nucleated at a velocity below the critical value ($\approx$35 μm s^{-1}, Fig. S1, ESI†). At a velocity above the critical value ($\approx$50 μm s^{-1}), the time decreases to around 1.0 s. These times are measured from the moment the central point of the domains enters the constriction until it exits. Regardless of the initial flow velocity, adding a constriction accelerates dowser domains and decreases their travel time compared to a microchannel without a constriction.

The graph in Fig. 2c summarizes the surface area of the dowser domains flowing in a linear microchannel with and without constriction. Without constriction, domains flowing below the critical velocity shrink in size (black dashed line) and disappear about 2.2 s after their formation (Fig. S1, ESI†).

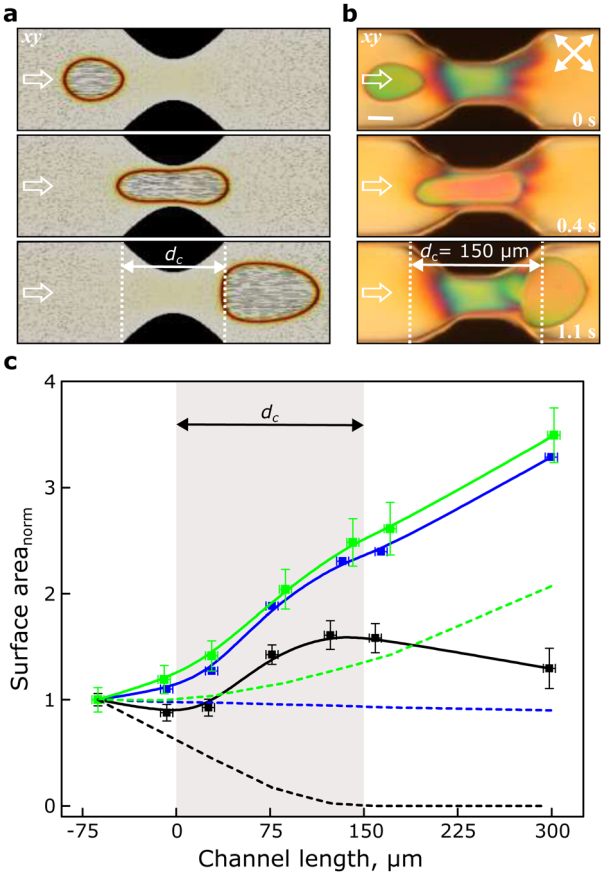

Fig. 2 Dowser domains in a microchannel constriction. (a) Numerical simulations predict significant changes in the shape of the domains as they flow through the channel constriction. (b) In experiments, a domain nucleated in a 100 μm wide linear microchannel at the critical velocity ($\approx$42 μm s^{-1}) passes through the constriction of length 150 μm in about 1.1 s. The time is measured from the moment the central point of the domain enters the constriction until it exits. The width of the constriction is about 40 to 50 μm. The scale bar is 25 μm. (c) The average surface area of domains flowing in the linear microchannel with (solid lines) and without (dashed lines) constriction. All domains are nucleated in a 100 μm wide linear channel at subcritical ($\approx$35 μm s^{-1}, black curves), critical ($\approx$42 μm s^{-1}, blue curves), and supercritical velocities ($\approx$50 μm s^{-1}, green curves). The domains accelerate significantly and grow as they flow through the channel constriction. The shaded region indicates the length of the constriction in the linear microchannel, $d_c \approx 150$ μm. The surface area is normalized to the initial size, which corresponds to the critical radii of the domains during their formation.

By adding the constriction, the domains grow (black solid line) and extend their lifetime to approximately 8 s (Fig. S1, ESI†). The critical velocity in the linear microchannel has no effect on the initial size and shape of dowser domains (blue dashed line). However, when they enter the constriction, their surface area increases to approximately 2.3 times their initial size (blue solid line). If the flow velocity is increased beyond the critical value, the domains expand even further and reach about 2.5 times their initial surface area after passing through the constriction. In contrast, the domains in the linear microchannel without constriction grow more gradually and only reach about 1.4 times their initial size when flowing at a velocity above the critical limit.

As the length of the constriction increases, the surface area of the domains increases further as they are exposed to a higher velocity for longer periods of time (Fig. S2, ESI†).

3.3. Dowser domains in expansion

Next, we examine the behavior of dowser domains as they flow through a square microfluidic expansion, where they experience effects opposite to those in the constriction. As shown in Fig. 3, the shape of the domain is significantly deformed when it enters an expansion whose width and length are twice that of the linear microchannel. Numerical simulations (Fig. 3a and Video S3, ESI†) reveal that the domain enlarges as it enters the expansion, and transitions from a circular to an ellipsoidal shape, with its long axis aligned with the flow. On its way to the center, the domain continues to expand along the direction of flow. Near the exit, it accelerates and continues to grow, maintaining its elongated shape. Experiments with a microchannel that expands from 100 μm to 200 μm (Fig. 3b and Video S4, ESI†) partially confirm these observations. In experiments, as the domain approaches the center of the expansion, it shrinks along the flow direction, while it expands perpendicular to it. Similar behavior can be observed in simulations, although it appears to occur earlier, immediately after entering the expansion (see Video S3, ESI†). On exiting the expansion, the domain accelerates and transitions from an elongated shape perpendicular to the flow to a shape aligned with the flow.

The flow velocity of the NLC decreases significantly in expansion, as can also be seen from experimental POM images in which changes in the birefringent colors can be observed (Fig. 3b and Video S4, ESI†). This decrease in velocity slows down the movement of the domain, which causes a slight change in the birefringent color from dark red to light red. The experimental analysis of the domains' surface area (Fig. 3c) and the temporal evolution of the position of the domains (Fig. S3, ESI†) show that domains that are entering 200 μm × 200 μm expansion from a 100 μm wide linear microchannel with velocity below the critical value undergo a symmetric reduction in size and are annihilated at the entrance. When entering the expansion at critical velocity, the domains continue to flow, but still annihilate near the center of the expansion (Fig. S3, ESI†). Only domains that enter at a velocity above the critical velocity persist throughout the expansion. As they flow through the expansion, these domains undergo dynamic shape transitions (Fig. 3a and b). The experiments show that the domains traverse the entire expansion in about 4.2 s, albeit with a significant suppression of growth. Although they leave the expansion smaller than when they entered it, they resume their growth afterwards, as both their radius and velocity remain above the critical value.

3.4. Changing the flow path of dowser domains

The shape and velocity of dowser domains can also be manipulated using serpentine microchannels in which the flow path undergoes periodic directional changes. Fig. 4a and b (Videos S5 and S6, respectively, ESI†) show numerical predictions of domain

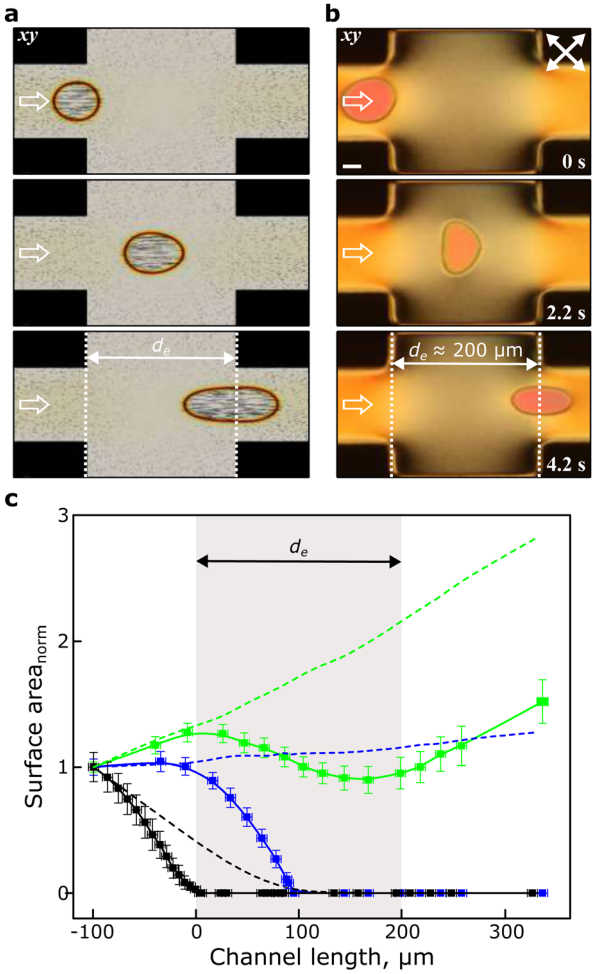

Fig. 3 Dowser domains in microchannel expansion. (a) Numerical simulations predict that the expansion significantly slows down and deforms dowser domains. (b) In experiments, a domain entering a 200 μm wide and 200 μm long expansion from a 100 μm wide linear channel with a velocity above the critical velocity takes about 4.2 s to flow through the entire expansion. The time is measured from the point at which the central point of the domain enters and until it leaves the expansion. The scale bar is 25 μm. (c) The average surface area of domains flowing in a linear microchannel with (solid lines) and without (dashed lines) expansion. All domains are nucleated in a linear 100 μm wide channel at subcritical (≈35 μm s^{-1}, black curves), critical (≈42 μm s^{-1}, blue curves), and supercritical velocities (≈50 μm s^{-1}, green curves). Domains flowing with the subcritical and the critical velocities are significantly decelerated and annihilate before they have travelled the entire length of the expansion. Only domains with a velocity above the critical velocity flow through the entire expansion. The shaded region indicates the position of the expansion in the linear microchannel, $d_e \approx 200$ μm. The surface area is normalized with the initial size, which corresponds to the critical radii of the domains when they are formed.

dynamics in serpentine microchannels with straight and curved bends, respectively. The corresponding experimental observations in 100 μm wide microchannels with curved bends are shown in Fig. 4c (Video S7, ESI†). Regardless of the geometry of the bend, the laminar velocity profile in serpentine microchannels exhibits a slight asymmetry, with the maximum velocity near the inner edge of each bend.[41,54] This asymmetry affects the orientation of the

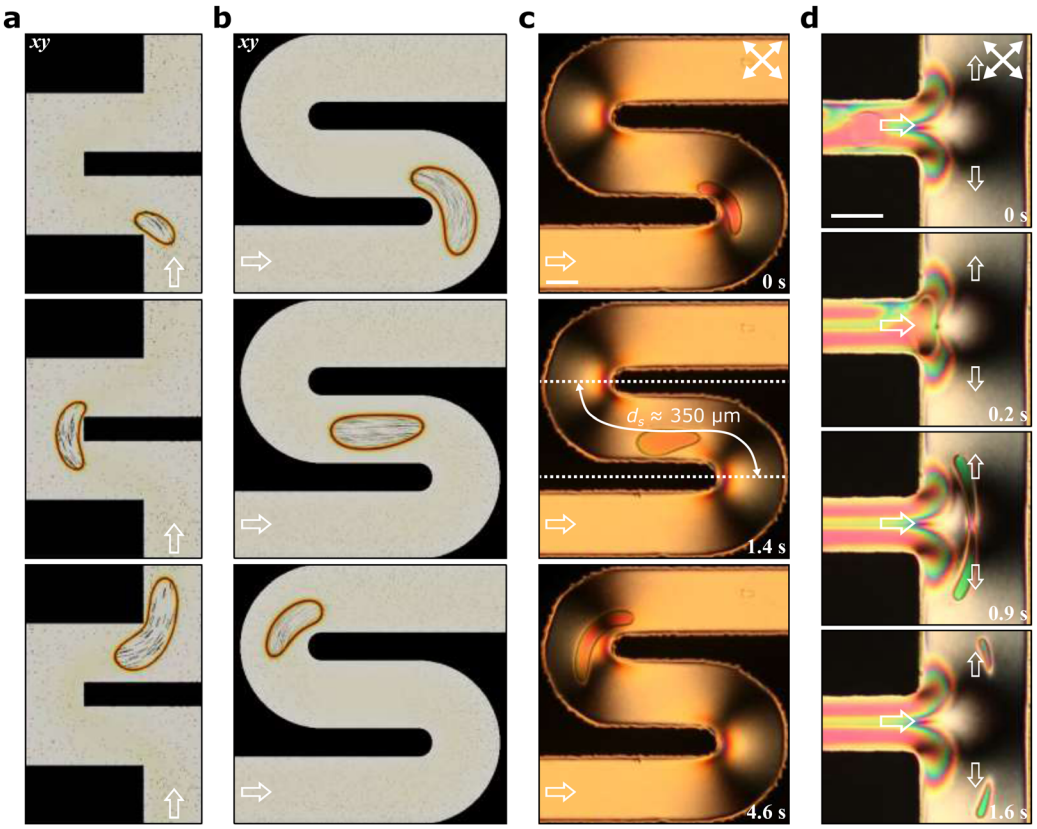

Fig. 4 Changing the path of flowing dowser domains. (a) and (b) Numerical simulations show how domains flow in serpentine microchannels with straight and curved bends, respectively. (c) Experimental observation of domains flowing in a serpentine microchannel. The bends accelerate and elongate the shape of the domains. (d) Experimental observation of a domain splitting into two smaller domains at the T-junction of the microchannel. The scale bars are 50 μm.

director field and leads to a gradual shift of the birefringent color. The velocity gradient drives the domains towards the inner part of the bends, where they are accelerated and adopt a curved shape. Between the bends, the domains elongate along the direction of flow and take on an elongated, rod-like shape.

Experiments show that curved bends in microchannels extend the lifetime of dowser domains when they transition from a 100 μm wide linear microchannel with subcritical velocity (Fig. S4, ESI†). When domains enter the bends at critical or supercritical velocities, they grow at two different rates, with faster growth occurring in the second bend. When leaving the curved regions, the domain surface increases by a factor of about 5 and 18 at critical and supercritical velocities, respectively. Compared to other channel geometries, the serpentine channel leads to a significantly stronger growth of the dowser domains in the case of a supercritical velocity.

Dowser domains can also split. As shown in the experiments in Fig. 4d (Video S8, ESI†), the domain can split into two smaller parts in a bifurcated T-junction microchannel where the LC flows from a single inlet into two symmetric side branches. At the junction, the flow expands the domain along the direction of the branches. If the flow is strong enough, the domain elongates to its maximum extent and eventually splits into two smaller daughter domains, which then enter the opposite branches. However, if the flow in the side branches is not strong enough, the domains shrink and annihilate. Symmetrical outlet branches facilitate the formation of daughter domains of the same size.

To achieve more precise control over domain dynamics, different microfluidic elements can be combined to form more complex channel architectures, as shown in Fig. 5. Fig. 5a (Video S9, ESI†) and Fig. 5b (Video S10, ESI†) show an example of an interconnected configuration consisting of two T-junctions connected by bent microchannels. In this case, upon entering the first T-junction, the dowser domain is symmetrically split into two smaller daughter domains, which then move separately. Despite the relatively lower flow velocity in the branched channels, the lifetime of the domains is extended at the channel bends so that they can reach the second T-junction. At this junction, the two domains merge back into a single domain. This configuration alllows controlled manipulation of the dowser domains so that they can be split at one point and later rejoined at another point, taking into account the specific design of the microchannels. In contrast, if the T-junction is asymmetric, *i.e.* one branch is significantly shorter than the other, the splitting process is suppressed and the domain flows intact through the longer branch (Fig. 5c and Video S11, ESI†).

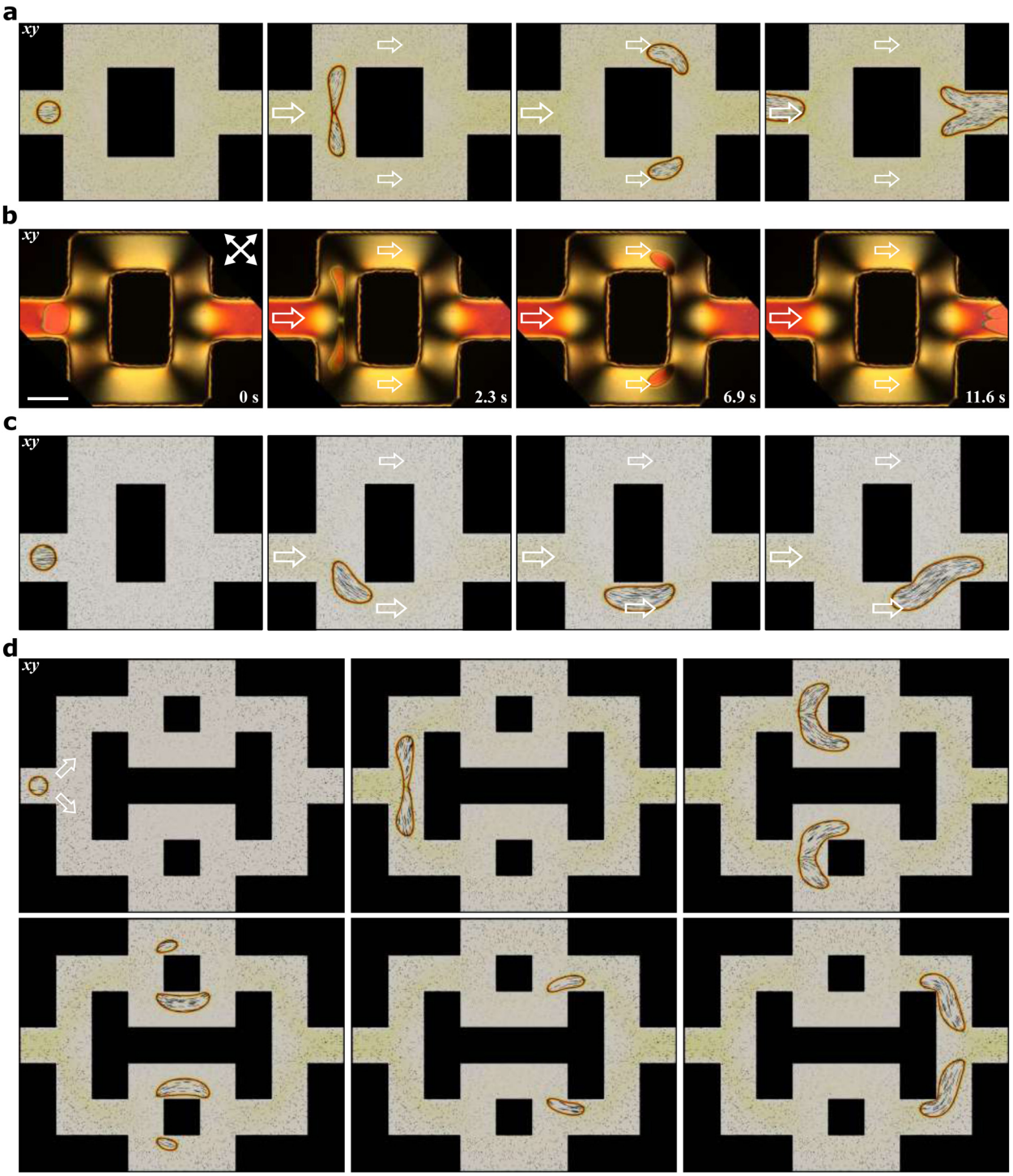

Fig. 5 Microfluidic circuit based on T-junctions and bend channels. (a) Numerical simulations and (b) experiments show that two T-junctions connected by bending channels allow symmetric splitting and merging of dowser domains. The scale bar is 100 μm. (c) If the side arms of a T-junction are not equal in length, splitting will not occur due to unequal velocities in the side arm channels. (d) T-junctions and curved channels can be connected to form a more hierarchical network that enables a parallel channel system with high throughput.

By strategically exploiting the interplay of fluid flow and geometry in T-junctions and curved microchannels, it is possible to construct highly organized microfluidic networks similar to electrical circuits (Fig. 5d and Video S12, ESI†).[56] These networks enable controlled and spatially resolved distribution of fluids and are particularly well suited to high-throughput applications, where a single input stream can be split into multiple branches arranged hierarchically across a wide channel network. Within this framework, dowser domains exhibit complex behaviors. An initial domain can split into two daughter domains at the first T-junction, which

can then continue downstream and undergo further splitting at subsequent junctions. Simulations show that with each additional T-junction, the division of the domains becomes increasingly asymmetric and produces both smaller and larger daughter domains. When a daughter domain becomes smaller than a critical size and the flow in the side branch falls below the critical value, the domain shrinks and eventually annihilates. In contrast, domains that remain above this threshold survive and continue in the network. The surviving domains are repeatedly split, reconfigured, and finally merge with each other. In the end, these domains merge into a single domain that is often larger than the original domain that entered the network.

Conclusions

In this paper, we demonstrate how microfluidic channels can precisely control the dynamics and structures of fluid flows. Our study shows that simply by varying the geometry of the microchannels, the behavior and shape of disclination loops with an escaped structure of NLC, the so-called ''dowser domains'', can be effectively manipulated. Different channel designs with their characteristic flow velocity profiles influence the dowser domains in a predictable and shapeable way by manipulating the local domain growth rate, which depends on the velocity and the local boundary curvature of the domain. All presented geometries significantly change the size and shape of the domains. Constrictions and serpentine channels accelerate dowser domains, leading to their enlargement. Channel expansions slow down the flow velocity, causing the domains to shrink. Other channel shapes can be easily designed to achieve the desired shape and size effects by utilizing the known mechanism of growth rate and disclination propagation. Furthermore, we show that a T-junction microchannel can split a domain into two daughter domains of equal size. By integrating T-junction channels with serpentine bends into more complex hierarchical networks, we can achieve programmable manipulation of dowser domains. The results presented here open avenues for the development of autonomous and automated flow control systems that could find applications in optofluidic technologies and other flow-based LC devices.

Conflicts of interest

There are no conflicts to declare.

Data availability

All data generated or analyzed during this study are included in this published article [and its ESI†].

Acknowledgements

The authors gratefully acknowledge the financial support of the Slovenian Research and Innovation Agency (ARIS) under contracts P1-0055 (T. E. and U. T.), P1-0099 (S. Č.), J1-50006 (S. Č.), J2-50092 (U. T.), and N1-0195 (S. Č.). The funding of the bilateral project BI-US/22-24-091 (T. E., J. J. dP., and U. T.) is also acknowledged. R. Z. acknowledges funding from Research Grants Council of Hong Kong *via* grant no. 16300221. J. J. dP. kindly acknowledges support from the U.S. Department of Energy, Materials Sciences, and Engineering Division.

References

1 A. D. Stroock, S. K. W. Dertinger, A. Ajdari, I. Mezic, H. A. Stone and G. M. Whitesides, *Science*, 2002, **295**, 647–651.
2 J. Atencia and D. J. Beebe, *Nature*, 2005, **437**, 648–655.
3 G. M. Whitesides, *Nature*, 2006, **442**, 368–373.
4 J. Deschamps, V. Kantsler, E. Segre and V. Steinberg, *Proc. Natl. Acad. Sci. U. S. A.*, 2009, **106**, 11444–11447.
5 R. L. Truby and J. A. Lewis, *Nature*, 2016, **540**, 371–378.
6 J. van der Gucht, M. Lemmers, W. Knoben, N. A. M. Besseling and M. P. Lettinga, *Phys. Rev. Lett.*, 2006, **97**, 108301.
7 X. Cheng, J. H. McCoy, J. N. Israelachvili and I. Cohen, *Science*, 2011, **333**, 1276–1279.
8 A. D. Rey, *J. Non-Newtonian Fluid Mech.*, 1996, **64**, 207–227.
9 O. Henrich, K. Stratford, P. V. Coveney, M. E. Cates and D. Marenduzzo, *Soft Matter*, 2013, **9**, 10243–10256.
10 A. Sengupta, U. Tkalec, M. Ravnik, J. M. Yeomans, C. Bahr and S. Herminghaus, *Phys. Rev. Lett.*, 2013, **110**, 048303.
11 Q. Zhang, W. Wang, S. Zhou, R. Zhang and I. Bischofberger, *Nat. Commun.*, 2024, **15**, 7.
12 L. Shang, Y. Cheng and Y. Zhao, *Chem. Rev.*, 2017, **117**, 7964–8040.
13 A. Huerre, V. Miralles and M.-C. Jullien, *Soft Matter*, 2014, **10**, 6888–6902.
14 N. Koumakis, E. Moghimi, R. Besseling, W. C. K. Poon, J. F. Brady and G. Petekidis, *Soft Matter*, 2015, **11**, 4640–4648.
15 J. Boschan, D. Vågberg, E. Somfai and B. P. Tighe, *Soft Matter*, 2016, **12**, 5450–5460.
16 N. M. Oliveira, S. Vilabril, M. B. Oliveira, R. L. Reis and J. F. Mano, *Mater. Sci. Eng.: C*, 2019, **97**, 851–863.
17 H. Amini, E. Sollier, M. Masaeli, Y. Xie, B. Ganapathysubramanian, H. A. Stone and D. D. Carlo, *Nat. Commun.*, 2013, **4**, 1826.
18 T. Emeršič, R. Zhang, Ž. Kos, S. Čopar, N. Osterman, J. J. De Pablo and U. Tkalec, *Sci. Adv.*, 2019, **5**, eaav4283.
19 S. Čopar, Ž. Kos, T. Emeršič and U. Tkalec, *Nat. Commun.*, 2020, **11**, 59.
20 G. Ilhan, L. N. Carenza and E. Bukusoglu, *Commun. Phys.*, 2025, **8**, 143.
21 P. de Gennes and J. Prost, *The Physics of Liquid Crystals, Oxford University Press, Inc.*, Oxford, 1995.
22 I. Dierking, *Textures of Liquid Crystals*, Wiley-VCH, 2003.
23 S. Fujii and O. Henrich, *Phys. Rev. E*, 2021, **103**, 052704.
24 S. Das, N. Atzin, X. Tang, A. Mozaffari, J. de Pablo and N. L. Abbott, *Phys. Rev. Lett.*, 2023, **131**, 098101.
25 S. Chandrasekhar and G. Ranganath, *Adv. Phys.*, 1986, **35**, 507–596.

26 C. Blanch-Mercader, P. Guillamat, A. Roux and K. Kruse, *Phys. Rev. Lett.*, 2021, **126**, 028101.
27 J. Brugués, J. Ignés-Mullol, J. Casademunt and F. Sagués, *Phys. Rev. Lett.*, 2008, **100**, 037801.
28 X. Wang, D. S. Miller, E. Bukusoglu, J. J. de Pablo and N. L. Abbott, *Nat. Mater.*, 2016, **15**, 106–112.
29 R. Zhang, S. A. Redford, P. V. Ruijgrok, N. Kumar, A. Mozaffari, S. Zemsky, A. R. Dinner, V. Vitelli, Z. Bryant, M. L. Gardel and J. J. de Pablo, *Nat. Mater.*, 2021, **20**, 875–882.
30 A. Sengupta, C. Bahr and S. Herminghaus, *Soft Matter*, 2013, **9**, 7251–7260.
31 L. Giomi, Ž. Kos, M. Ravnik and A. Sengupta, *Proc. Natl. Acad. Sci. U. S. A.*, 2017, **114**, E5771–E5777.
32 Q. Zhang, R. Zhang, B. Ge, Z. Yaqoob, P. T. C. So and I. Bischofberger, *Proc. Natl. Acad. Sci. U. S. A.*, 2021, **118**, e2108361118.
33 O. Wiese, D. Marenduzzo and O. Henrich, *Soft Matter*, 2016, **12**, 9223–9237.
34 D. Forster, T. C. Lubensky, P. C. Martin, J. Swift and P. S. Pershan, *Phys. Rev. Lett.*, 1971, **26**, 1016–1019.
35 F. M. Leslie, in *Theory of Flow Phenomena in Liquid Crystals*, ed. G. H. Brown, *Advances in Liquid Crystals*, Academic New York, 1979.
36 S. A. Jewell, S. L. Cornford, F. Yang, P. S. Cann and J. R. Sambles, *Phys. Rev. E*, 2009, **80**, 041706.
37 H. Stark, *Phys. Rep.*, 2001, **351**, 387–474.
38 A. Córdoba, T. Stieger, M. G. Mazza, M. Schoen and J. J. de Pablo, *J. Rheol.*, 2016, **60**, 75–95.
39 R. G. Sumesh, P. Thampi and J. M. Yeomans, *Mol. Phys.*, 2015, **113**, 2656–2665.
40 A. Sengupta, C. Pieper, J. Enderlein, C. Bahr and S. Herminghaus, *Soft Matter*, 2013, **9**, 1937–1946.
41 K. Fedorowicz, R. Prosser and A. Sengupta, *Soft Matter*, 2023, **19**, 7084–7092.
42 A. N. Beris and B. J. Edwards, *et al.*, *Thermodynamics of Flowing Systems: with Internal Microstructure*, Oxford University Press, 1994.
43 C. Denniston, E. Orlandini and J. M. Yeomans, *Phys. Rev. E*, 2001, **63**, 056702.
44 M. Ravnik and S. Žumer, *Liq. Cryst.*, 2009, **36**, 1201–1214.
45 R. Zhang, T. Roberts, I. S. Aranson and J. J. De Pablo, *J. Chem. Phys.*, 2016, **144**, 084905.
46 V. M. Batista, M. L. Blow and M. M. T. da Gama, *Soft Matter*, 2015, **11**, 4674–4685.
47 J. Fukuda, H. Yokoyama, M. Yoneya and H. Stark, *Mol. Cryst. Liq. Cryst.*, 2005, **435**, 63–723.
48 Z. Guo and C. Shu, *Lattice Boltzmann Method and Its Application in Engineering*, World Scientific, 2013, vol. 3.
49 W. Wang and R. Zhang, *Crystals*, 2021, **11**, 1071.
50 M. Kleman and O. D. Lavrentovich, *Soft Matter Physics: An Introduction*, Springer, 2003.
51 J. L. Ericksen, *Mol. Cryst. Liq. Cryst.*, 1969, **7**, 153–164.
52 F. M. Leslie, *Q. J. Mech. Appl. Math.*, 1966, **19**, 357–370.
53 O. Parodi, *J. Phys.*, 1970, **31**, 581–584.
54 K. Fedorowicz and R. Prosser, *Phys. Fluids*, 2022, **34**, 063106.
55 A. Sengupta, S. Herminghaus and C. Bahr, *Appl. Phys. Lett.*, 2012, **101**, 164101.
56 K. W. Oh, K. Lee, B. Ahn and E. P. Furlani, *Lab Chip*, 2012, **12**, 515–545.